Near to short wave infrared light generation through AlGaAs-on-insulator nanoantennas

Marco Gandolfi,[1,2,3,*] Luca Carletti,[1,2,3] Andrea Tognazzi,[2,4] Alfonso C. Cino,[4] Costantino De Angelis,[1,2,3] and Massimiliano Guasoni[5]

[1] *Dipartimento di Ingegneria dell'Informazione, Università degli Studi di Brescia, Via Branze 38, 25123 Brescia, Italy*
[2] *Consiglio Nazionale delle Rircerche - Istituto Nazionale di Ottica, Via Branze 45, 25123 Brescia, Italy*
[3] *Consorzio Nazionale Interuniversitario per le Telecomunicazioni (CNIT), Viale G.P. Usberti 181/A Sede Scientifica di Ingegneria-Palazzina 3, 43124 Parma, Italy*
[4] *Dipartimento di Ingegneria - Università degli Studi di Palermo, Viale delle Scienze ed. 10, Palermo, 90128, Italy*
[5] *Optoelectronics Research Centre, University of Southampton, Southampton, University Road West Highfield Campus B46, Southamption, SO17 1BJ, United Kingdom*
[*] *marco.gandolfi1@unibs.it*

Abstract: AlGaAs-on-insulator (AlGaAs-OI) has recently emerged as a novel promising platform for nonlinear optics at the nanoscale. Among the most remarkable outcomes, second-harmonic generation (SHG) in the visible/near infrared spectral region has been demonstrated in AlGaAs-OI nanoantennas (NA). In order to extend the nonlinear frequency generation towards the short wave infrared window, in this work we propose and demonstrate via numerical simulations difference frequency generation (DFG) in AlGaAs-OI NAs. The NA geometry is finely adjusted in order to obtain simultaneous optical resonances at the pump, signal and idler wavelengths, which results in an efficient DFG with conversion efficiencies up to 0.01%. Our investigation includes the study of the robustness against random variations of the NA geometry that may occur at fabrication stage. Overall, these outcomes identify a new potential and yet unexplored application of AlGaAs-OI NAs as compact devices for the generation and control of the radiation pattern in the near to short infrared spectral region.

1. Introduction

In the last few years AlGaAs-on-insulator (AlGaAs-OI) has emerged as a novel promising platform for nonlinear optics [1–7]. Differently from standard AlGaAs devices grown on their native GaAs substrate, AlGaAs-OI benefits from a low-index cladding that allows for strong mode confinement, which in turn enhances the optical nonlinear response of AlGaAs [8–11]. Among the AlGaAs-OI devices of interest for nonlinear optics, we can distinguish between long (few millimetres/centimetres) waveguides, fabricated via wafer bonding and electron beam lithography [12], and compact (sub-micron to few microns long) nanoantennas (NAs), typically fabricated via molecular beam epitaxy [13]. While phase matching is the leading mechanism to achieve relevant nonlinear conversion in waveguides, in NAs the nonlinear processes are boosted by cavity resonances at the involved wavelengths [8].

Recently, AlGaAs-OI NAs have been proposed to mold and tune the radiation pattern of second-harmonic generation (SHG) at the nanoscale in the visible/near-infrared region of the electromagnetic spectrum ($\sim$ 800 nm) [14–18]. Indeed, in contrast with the plasmonic counterpart, this all-dielectric solution combines large nonlinearities and low optical losses.

An exciting but yet unexplored evolution of these outcomes is light generation in the near/short wave infrared (wavelengths beyond 1400 nm) via difference frequency generation (DFG). This spectral region is important for applications ranging from medicine and biology to telecommunications [19]. While substantial near/mid-infrared generation through DFG has been reported in standard few centimeters long $LiNbO_3$ [20] and AlGaAs waveguides [21, 22], to the best of our knowledge there has been little to no attempt to demonstrate DFG in compact sub-micrometer or few-micrometers long all-dielectric devices. Inspired by the recent achievements in SHG and spontaneous parametric down-conversion (SPDC) [23], in this manuscript we report on the design of compact AlGaAs NAs for near/short wave infrared generation through DFG. The envisaged

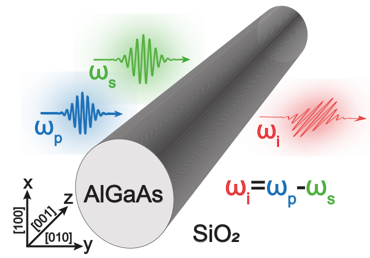

Fig. 1. Sketch of the setup: the incident pump (blue) and signal (green) plane waves propagate along the y direction and are $x-$polarised. The idler radiation (red) is generated via difference frequency generation and is z-polarized. The Cartesian coordinate system in the figure shows the orientation of the crystal axes of AlGaAs.

setup is sketched in Fig. 1, where two intense beams, conventionally named pump and signal, illuminate the NA and generate a new wavelength, named idler, through DFG. Differently from the case of SHG, which requires resonances at the fundamental and the second-harmonic frequencies, the design of NAs for DFG is further complicated by the requirement of resonances at all the three frequencies into play [24]. Section 2 is dedicated to the design of NAs that are simultaneously resonant at pump, signal and idler. In Section 3, the nonlinear system of equations coupling pump, signal and idler is solved numerically taking into account the anisotropic second-order nonlinear response of AlGaAs, and we identify the most suitable configurations to maximise idler generation. Finally in Section 4, we discuss the robustness of our method against fabrication imperfections by showing how the variation of the geometrical parameters may affect the DFG conversion efficiency (CE).

2. Resonance analysis

We consider a cylindrical AlGaAs NA with its axis oriented along the longitudinal direction z and fully embedded in an insulator. Among the possible choices for the cladding, silica [25] and hydrogen silsesquioxane (HSQ) [10, 12] stand out for their low index. For the sake of exemplification, here we focus on silica, but the present results might be readily generalized to HSQ cladding, the latter yielding a similar refractive index. We assume that the incident beams size is substantially larger than the NA dimensions, so that the beams can be modelled as plane waves. Pump and signal beams with angular frequencies ω_p and ω_s illuminate the NA. We focus on the case where the illumination occurs laterally, i.e. the wave-vectors of the incident plane waves are parallel to the y-direction and the electric fields are polarized along x, as displayed in Fig. 1. In this way, by exploiting the length of the NA we maximize the illuminated surface and the total energy that can be converted by DFG. Moreover, we assume that the antenna length L is substantially larger than its transverse dimension d ($L/d \gg 1$) and the wavelengths into play ($L/\lambda \gg 1$), therefore a few-microns long at least. Note that, for notation simplicity, despite this assumption here we still use the term "nanoantenna". Similarly to slab waveguides, which are characterised by ratios $L/d \gg 1$, $L/\lambda \gg 1$ and are therefore approximated as infinite in the length direction, so in the case under investigation we can approximate the antenna as a 2D object (in the x-y plane) with indefinite length along the z-direction, which on its turn reduces the numerical load and simplifies the interpretation of the results. In order to further simplify the

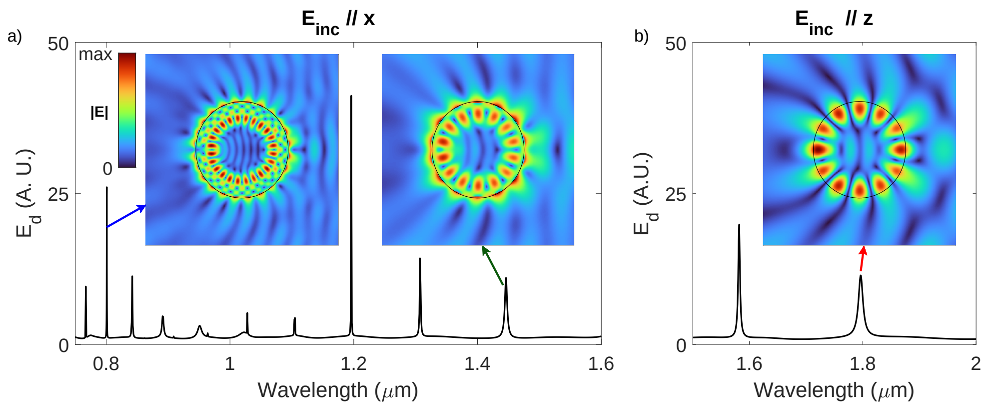

Fig. 2. Electromagnetic energy density (E_d) stored within the circular NA (r = 740 nm) when excited by a x-polarised (panel a) or z-polarised (panel b) plane wave. The insets display the norm of the electric field at the pump (λ = 801 nm, blue arrow), signal (λ = 1446 nm, green arrow) and idler (λ = 1796 nm, red arrow) resonances.

complex numerical design, we limit our investigation to antennas with circular cross-sections and a sub-micron radius.

The interaction between the scattered pump and signal fields inside the NA generates the idler (angular frequency ω_i) via DFG. The crystalline axes of the AlGaAs are aligned with the reference frame reported in Fig. 1. AlGaAs has a nonlinear second-order susceptibility tensor $\chi^{(2)}_{ijk}$ = 100 pm/V if $i \neq j \neq k$, and $\chi^{(2)}_{ijk} = 0$ otherwise [8].

We look for those NA cross-sections that exhibit three resonances at the pump, signal and idler frequencies and that satisfy the DFG energy conservation relation:

$$\omega_i = \omega_p - \omega_s. \tag{1}$$

Note that in the following we use interchangeably the frequencies $\omega_{p,s,i}$ and the corresponding wavelengths $\lambda_{p,s,i} = 2\pi c/\omega_{p,s,i}$ (c being the speed of light in free space).

To find the suitable resonances, we use finite element simulations (COMSOL Multiphysics) [26–31] to calculate the electromagnetic energy density per unit length (E_d) stored in the NA as a function of wavelength, when the NA is excited by a x-polarised plane wave (Fig. 2a). The peaks of the stored energy density identify the available pump and signal resonances.

According to the AlGaAs nonlinear tensor ($\chi^{(2)}_{ijk} \neq 0$ for $i \neq j \neq k$), a non-zero z-component of the scattered signal or pump electric field would be required in order to have a non-zero x or y- component of the idler electric field. However, in the 2D geometry under study with lateral illumination, the z-component of the signal and pump is null. Therefore, the generated idler electric field has null x and y component, namely, it is oriented parallel to the z-axis. In Fig. 2b we report the energy density corresponding to an excitation with a z-polarised plane wave, from which we identify the idler resonances that are potentially available for the DFG process. The refractive indices of the $Al_\xi Ga_{1-\xi}As$ core and the silica cladding are taken from [32] and [33], respectively, $\xi \approx 0.2$ being the standard value used in SHG processes to minimize the optical losses when the pump is at telecom wavelengths ($\sim$ 1550 nm).

Here, we report a NA with circular cross-section and with three resonances at the frequencies satisfying the condition in Eq. 1. Indeed, when the NA radius is r = 740 nm, pump, signal and idler resonances are at wavelengths of 801 nm, 1446 nm and 1796 nm, respectively, as highlighted by the arrows in Fig. 2. As it can be seen from the electric field profile reported in the insets in Fig. 2, the three resonances correspond to Whispering Gallery Modes (WGMs) and thus present higher quality factors with respect to usual Mie-type resonances in dielectric NAs [8,13]. Indeed, the quality factor $Q_j = \omega_j/\Delta\omega_j$ (with $j = p, s, i$ and $\Delta\omega_j$ being the resonance line-width), is 2000, 300 and 1800 at the pump, signal and idler frequencies, respectively.

3. DFG Conversion Efficiency

In this section, we discuss a fully-coupled numerical model implemented with finite element method to simulate the DFG process and then to compute the idler CE in the above-mentioned circular NA. An extensive description of the model is provided in Ref. [22]. The Maxwell's

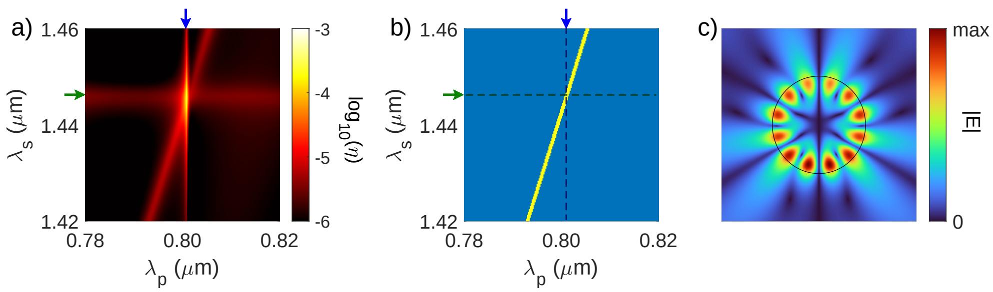

Fig. 3. a) DFG CE η (the logarithm is used to highlight the contrast) as function of the signal and pump wavelengths. The pump and signal incident intensity is $I_p = I_s = 1$ GW/cm^2. The blue and green arrows on the top and on the left side indicate the resonant wavelengths for pump (801 nm) and signal (1446 nm), respectively. b) Plane as in panel a) displaying the regions where the corresponding idler wavelength $\lambda_i = (\lambda_p^{-1} - \lambda_s^{-1})^{-1}$ is close to its resonance (i.e. in the range 1796 ± 2 nm), highlighted with a yellow stripe, or far from the resonance (blue). c) Generated electric field (norm) of the idler when $\lambda_p = 801$ nm and $\lambda_s = 1446$ nm. A circular NA with radius $r = 740$ nm is considered here.

equations describing the evolution of the electric field $\mathbf{E}$ at the pump, signal and idler frequencies read as:

$$\nabla \times (\nabla \times \mathbf{E}(\omega_n)) - k_0^2(\omega_n)\,\varepsilon_r \mathbf{E}(\omega_n) = \mu_0 \omega_n^2 \mathbf{P}^{(2)}(\omega_n)\,, \tag{2}$$

with $n = p, s, i$. The 3 frequencies are coupled through the quadratic nonlinear polarization vector $\mathbf{P^{(2)}}$, which for AlGaAs reads as:

$$\begin{cases} P_a^{(2)}(\omega_p) = \varepsilon_0 \chi^{(2)} \left[E_b(\omega_s)E_c(\omega_i) + E_c(\omega_s)E_b(\omega_i)\right] \\ P_a^{(2)}(\omega_s) = \varepsilon_0 \chi^{(2)} \left[E_b(\omega_p)E_c^*(\omega_i) + E_c(\omega_p)E_b^*(\omega_i)\right] \\ P_a^{(2)}(\omega_i) = \varepsilon_0 \chi^{(2)} \left[E_b(\omega_p)E_c^*(\omega_s) + E_c(\omega_p)E_b^*(\omega_s)\right], \end{cases} \tag{3}$$

where $a, b, c \in \{x, y, z\}$, with $a \neq b \neq c$. The incident field for pump and signal is represented by x-polarised plane waves with intensities I_p and I_s, respectively. On the other hand, the incident idler field is null; idler is indeed generated as a result of the nonlinear coupling among pump and signal inside the NA.

In analogy with the case of SHG reported in [8], the CE is defined as the ratio of the generated idler power to the total (signal + pump) incident power. In the system under analysis the NA exhibits translation symmetry along the z-direction, therefore the efficiency reduces to the following formula:

$$\eta = \frac{\oint_\gamma \mathbf{S}(\omega_i) \cdot \mathbf{n}\, d\gamma}{2r(I_s + I_p)}. \tag{4}$$

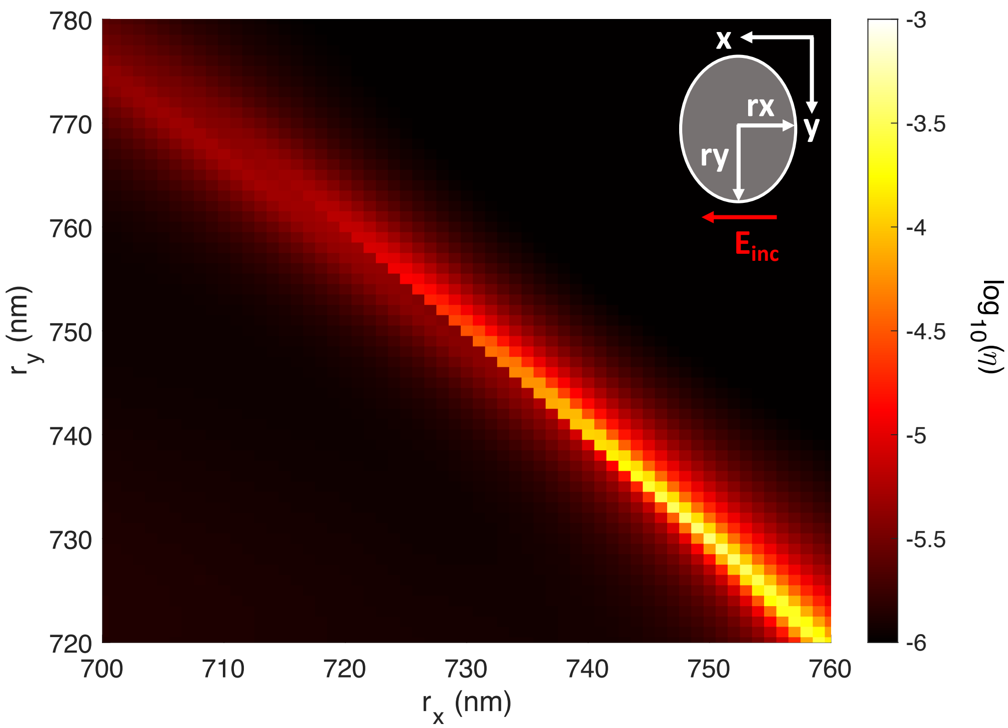

Fig. 4. DFG CE η (the logarithm is used to highlight the contrast) as function of the two ellipse semi-axes r_x and r_y. The wavelength of the incident pump and signal is fixed to 801 nm and 1446 nm, respectively. The intensity of both beams is set to 1 GW/cm^2. Inset: Sketch of the elliptic nanoantenna and the illuminating electric field (E_{inc}).

where $\mathbf{S}(\omega_i)$ is the Poynting vector at the idler frequency, γ is a closed line containing the NA circular cross section and $\mathbf{n}$ is the normal unit vector pointing outside the adopted closed line.

In Fig. 3a we report η as function of the pump (λ_p) and signal (λ_s) wavelengths when pump and signal intensities are $I_s = I_p = 1$ GW/cm^2. It is worth noting that this or even higher values (1-10 GW/cm^2) of intensity have been employed for efficient second-harmonic generation in NAs [13, 16, 34, 35]. Three bright striped regions stand out where the DFG conversion is remarkable. The vertical and horizontal stripes are centered around the pump and signal resonances. This is not surprising, as the DFG is boosted by the enhanced electric field of both pump and signal when they are resonant. Similarly, the diagonal stripe turns out to be the region where the idler is resonant. Indeed, in Fig. 3b we plot in yellow the region of the plane (λ_p, λ_s) where the idler wavelength $\lambda_i = (\lambda_p^{-1} - \lambda_s^{-1})^{-1}$ is in the range 1796 ± 2 nm, that is to say, close to the idler resonance. We observe that the yellow region in Fig. 3b matches well the bright diagonal stripe of Fig. 3a. In conclusion, Fig. 3a shows that the DFG conversion is enhanced when any of the pump, signal or idler wavelength is resonant. On the other hand, the peak of conversion is obtained when pump, signal and idler are simultaneously resonant, namely, at the intersection between the 3 bright striped regions. For the considered NA, this occurs for $\lambda_p = 801$ nm and $\lambda_s = 1446$ nm (corresponding to $\lambda_i = 1796$ nm). Consequently, the shape of the generated idler field, reported in Fig. 3c, matches well with the field in the inset of Fig. 2b, thus proving that the DFG process we propose relies on three resonant modes of the NAs. The achieved maximum CE $\eta_{max} \sim 2.5 \times 10^{-4}$ is in line with the CE previously obtained for SHG processes when similar values of pump intensity are employed [13].

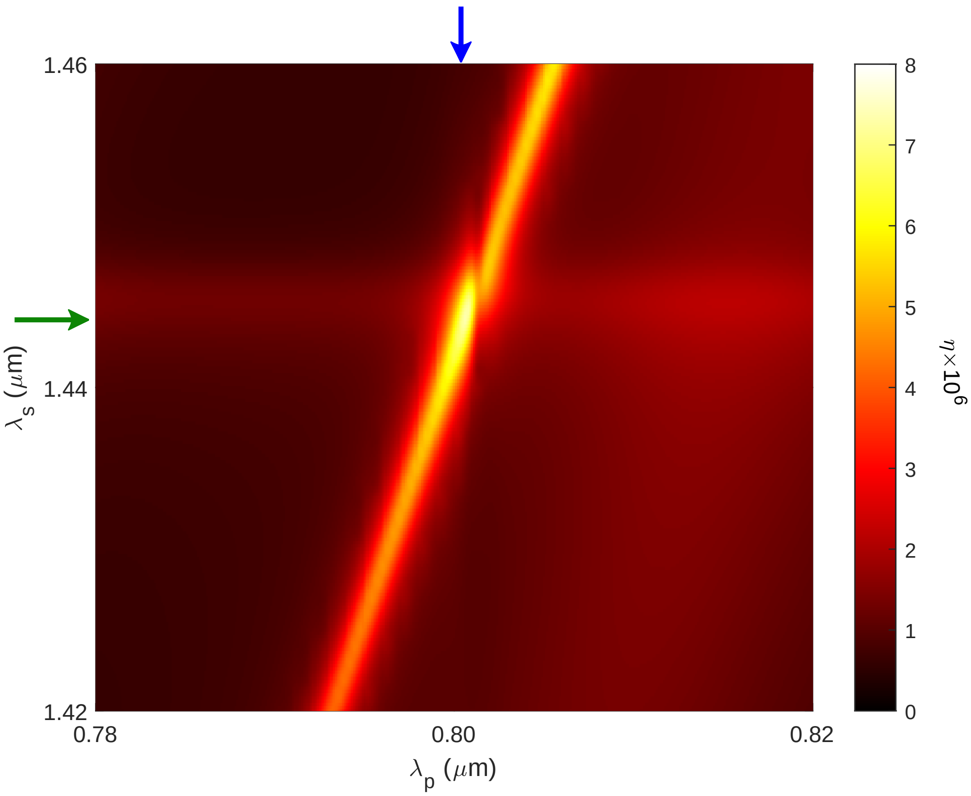

Fig. 5. DFG CE η as a function of the signal and pump wavelengths, for an elliptical NA with r_x = 720 nm and r_y = 760 nm. The pump and signal incident intensity is $I_p = I_s$ = 1 GW/cm^2. The blue and green arrows on the top and on the left side indicate the resonant wavelengths for pump (801 nm) and signal (1446 nm), respectively.

4. Conversion efficiency robustness upon variation of the geometrical parameters

In this section, we discuss how the variation of the geometrical parameters of the NA affects the CE. In particular, due to experimental tolerances, it is quite challenging to fabricate a perfectly circular NA, but rather an elliptical NA is more likely. For this reason, in this section we consider the CE generated by an elliptical NA, whose semi-axes are r_x and r_y (as schematized in the inset of Fig. 4). In Fig. 4, we report the CE as function of r_x and r_y. The incident pump and signal are polarized along x, their wave vector is parallel to y, their intensity is 1 GW/cm^2 and their wavelengths are 801 nm and 1446 nm, respectively.

When $r_x = r_y$ = 740 nm we recover the circular NA described in the previous sections and the CE is high. Moreover, we note that the CE can be even further enhanced up to 3.9×10^{-4} for r_x = 750 nm and r_y = 730 nm. On the other hand, this remarkable CE comes at the expenses of a strong sensitivity to small variations of the geometric parameters. For example, we observe that the CE drops by 2 orders of magnitude if r_x = 755 nm and and r_y = 730, reaching the value of $\eta = 7 \times 10^{-6}$. For this reason, these very efficient configurations are quite sensitive to fabrication imperfections and a small variation on the geometry may considerably reduce the CE.

A possible way to overcome this problem is to move towards the top left corner of Fig. 4, i.e. semi-axes $r_x \sim$ 720 nm and $r_y \sim$ 760 nm. Despite in this region the CE is lower ($\eta < 10^{-5}$), however it is weakly affected by semi-axes variations as large as 10 nm. The map of the CE

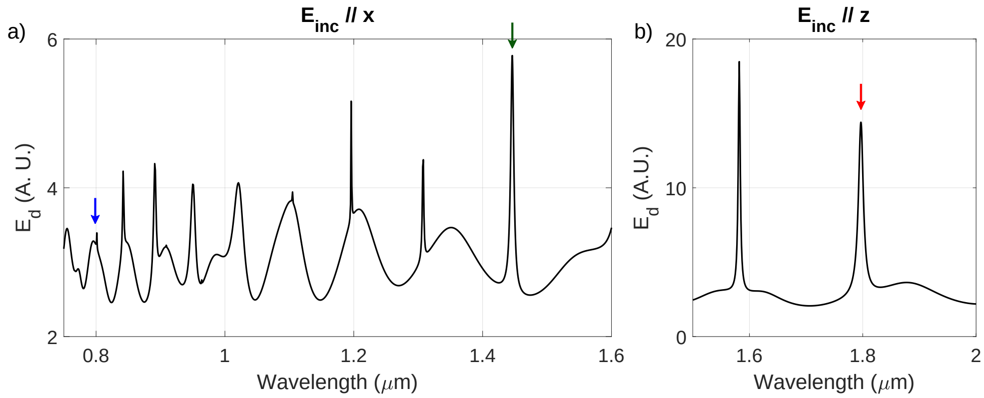

Fig. 6. Electromagnetic energy density (E_d) stored within the elliptical NA (r_x = 720 nm and r_y = 760 nm) when the NA is excited by a x-polarised (panel a) or z-polarised (panel b) plane wave. The blue, green and red arrows identify the pump (λ = 801 nm), signal (λ = 1446 nm) and idler (λ = 1796 nm) resonances.

as function of the pump and signal wavelengths for the case r_x = 720 nm and r_y = 760 nm is reported in Fig. 5. As for the case illustrated in Fig. 3a, the bright diagonal stripe corresponds to a resonant idler. However, differently from Fig. 3a, pump and signal resonances have a minor impact on the CE. Indeed, the CE computed when the idler is resonant but the pump and signal are not is of the same order of magnitude (only 2 times smaller) than the case where pump, signal and idler are simultaneously resonant (blue and green arrows in Fig. 5). The latter trend may be explained by looking at the electromagnetic energy density (E_d) stored at pump, signal and idler wavelengths, calculated with linear simulations (Fig. 6). While for pump and signal E_d varies by a factor of 2 outside the respective resonances (as depicted in Fig. 6a), on the contrary the variation is substantial in the case of the idler (e.g. about a factor 7 between wavelengths at 1796 nm and at 1750 nm, see Fig. 6b). On the other hand, in the efficient case in Fig. 3a all the three resonances showed an energy density changing more than one order of magnitude passing from the maximum to the minimum. Thus, the efficient case is also more sensitive to small variations of the geometry than the design reported in Fig. 5.

5. Conclusion

AlGaAs-OI has recently emerged as a promising platform for nonlinear nano-optics. In the last few years, several works have addressed second-harmonic generation, sum-frequency generation and spontaneous parametric down conversion in the visible/near-infrared spectrum by means of AlGaAs-OI NAs. In this paper we extended the operation in the near/short wave infrared spectral region via DFG.

We identified a NA with circular cross-section exhibiting simultaneous resonances at three distinct wavelengths that satisfy the DFG energy conservation relation. The corresponding CE is comparable with the CE obtained via SHG processes [13].

We investigated how the variation of the geometrical parameters may affect the CE. The latter seems to be substantially sensitive to variations of a few nanometers in the case of multi-resonant NA, which may pose a challenge at fabrication stage. However, we have identified a further configuration based on an elliptical NAs where the idler resonance is dominant, which is characterized by a lower CE but is remarkably more robust against geometrical perturbations.

We have focused our investigation on the special case where the NA length is substantially larger than the diameter and the wavelengths into play ($L/d \gg 1$, $L/\lambda \gg 1$), which allows employing a 2D representation that drastically reduces the computational cost. AlGaAs nanowires represent an example where the above-mentioned conditions ($L/d \gg 1$, $L/\lambda \gg 1$) apply [36, 37]. In addition, our analysis could be easily adapted to NAs with arbitrary shape, which paves the way for further scenarios. For example, AlGaAs NAs with rectangular base and arbitrary ratio $L/d_{1,2} \gg 1$ ($d_{1,2}$ being the transverse dimensions) could be fabricated on-chip via standard techniques used for integrated waveguides [10, 11, 25]. In this case, lateral illumination and DFG characterisation could be achieved either via free-space coupling [38] or via a dedicated coupling system based on integrated tapers and/or gratings.

Note that a full 3D numerical investigation would follow the same logic as in the 2D case discussed in this work. For example, in the case of NAs with circular base, the search for the resonant wavelengths would be done as a function of both the NA radius and length, and for illumination with arbitrary tilt angle. However, the main challenge in the 3D case is represented by the computational cost, which makes the analysis prohibitively time consuming for the computational resources at our disposal.

In conclusion, these outcomes identify a new potential application of AlGaAs-OI NAs as compact devices for the generation and control of light in the near to short wave infrared spectral region. We expect that resorting to different or more complex geometries (*e.g.*, NA with rectangular cross-section, coupled NAs, arrays or metasurfaces) one may further increase the efficiency and spectral tunability of the generated radiation, even reaching DFG generation in the mid-infrared region. Our results illustrate potential for the design of quantum photonic structures via DFG-SPDC reciprocity [39, 40] and for the development of new nanoscale sources of light at near-short infrared frequencies.

Funding. We acknowledge the European Union Horizon 2020 Research and Innovation program under Grant Agreement No. 899673; the Italian Ministry of University and Research (MIUR) through the PRIN project METEOR Grant No. 2020EY2LJT_002; the Italian Ministry of University and Research (MIUR) through the PRIN project NOMEN Grant No. 2017MP7F8F; the Russian Science Foundation grant No. 22-12-00204. M. Guasoni acknowledges funding from the European Research Council under the H2020 Programme (ERC Starting Grant No. 802682) and from the UK Engineering and Physical Sciences Research Council EPSRC (grant EP/T019441/1).

Acknowledgments. M. Gandolfi and A. Tognazzi acknowledge the European Union for the financial support through "FESR o FSE, PON Ricerca e Innovazione 2014-2020 - DM 1062/2021". A. Tognazzi acknowledges the financial support from the University of Palermo through "Fondo Finalizzato alla Ricerca di Ateneo 2023 (FFR2023)".

Disclosures. The authors declare no conflicts of interest.

Data Availability Statement. Data underlying the results may be obtained from the authors upon reasonable request.

Supplemental document. No Supplemental document available.

References

1. M. Rahmani, G. Leo, I. Brener, A. V. Zayats, S. A. Maier, C. De Angelis, H. Tan, V. F. Gili, F. Karouta, R. Oulton *et al.*, "Nonlinear frequency conversion in optical nanoantennas and metasurfaces: materials evolution and fabrication," Opto-Electronic Adv. **1**, 180021–1 (2018).
2. S. Liu, M. B. Sinclair, S. Saravi, G. A. Keeler, Y. Yang, J. Reno, G. M. Peake, F. Setzpfandt, I. Staude, T. Pertsch *et al.*, "Resonantly enhanced second-harmonic generation using III–V semiconductor all-dielectric metasurfaces," Nano letters **16**, 5426–5432 (2016).
3. S. S. Kruk, R. Camacho-Morales, L. Xu, M. Rahmani, D. A. Smirnova, L. Wang, H. H. Tan, C. Jagadish, D. N. Neshev, and Y. S. Kivshar, "Nonlinear optical magnetism revealed by second-harmonic generation in nanoantennas," Nano letters **17**, 3914–3918 (2017).
4. B. Sain, C. Meier, and T. Zentgraf, "Nonlinear optics in all-dielectric nanoantennas and metasurfaces: a review," Adv. Photonics **1**, 024002 (2019).
5. K. Frizyuk, I. Volkovskaya, D. Smirnova, A. Poddubny, and M. Petrov, "Second-harmonic generation in Mie-resonant dielectric nanoparticles made of noncentrosymmetric materials," Phys. Rev. B **99**, 075425 (2019).

6. G. Grinblat, “Nonlinear dielectric nanoantennas and metasurfaces: frequency conversion and wavefront control,” ACS Photonics **8**, 3406–3432 (2021).
7. A. Krasnok, M. Tymchenko, and A. Alù, “Nonlinear metasurfaces: a paradigm shift in nonlinear optics,” Mater. Today **21**, 8–21 (2018).
8. L. Carletti, A. Locatelli, O. Stepanenko, G. Leo, and C. De Angelis, “Enhanced second-harmonic generation from magnetic resonance in AlGaAs nanoantennas,” Opt. Express **23**, 26544–26550 (2015).
9. B. Kuyken, M. Billet, F. Leo, K. Yvind, and M. Pu, “Octave-spanning coherent supercontinuum generation in an AlGaAs-on-insulator waveguide,” Opt. Lett. **45**, 603–606 (2020).
10. S. May, M. Kues, M. Clerici, and M. Sorel, “Second-harmonic generation in AlGaAs-on-insulator waveguides,” Opt. Lett. **44**, 1339–1342 (2019).
11. S. May, M. Clerici, and M. Sorel, “Supercontinuum generation in dispersion engineered algaas-on-insulator waveguides,” Sci. Reports **11**, 2052 (2021).
12. L. Ottaviano, M. Pu, E. Semenova, and K. Yvind, “Low-loss high-confinement waveguides and microring resonators in AlGaAs-on-insulator,” Opt. Lett. **41**, 3996–3999 (2016).
13. V. F. Gili, L. Carletti, A. Locatelli, D. Rocco, M. Finazzi, L. Ghirardini, I. Favero, C. Gomez, A. Lemaître, M. Celebrano *et al.*, “Monolithic AlGaAs second-harmonic nanoantennas,” Opt. Express **24**, 15965–15971 (2016).
14. E. V. Melik-Gaykazyan, K. L. Koshelev, J.-H. Choi, S. S. Kruk, H.-G. Park, A. A. Fedyanin, and Y. S. Kivshar, “Enhanced second-harmonic generation with structured light in AlGaAs nanoparticles governed by magnetic response,” JETP Lett. **109**, 131–135 (2019).
15. P. P. Vabishchevich, S. Liu, M. B. Sinclair, G. A. Keeler, G. M. Peake, and I. Brener, “Enhanced second-harmonic generation using broken symmetry III–V semiconductor fano metasurfaces,” Acs Photonics **5**, 1685–1690 (2018).
16. A. Tognazzi, P. Franceschini, D. Rocco, L. Carletti, A. Locatelli, M. Gandolfi, D. Zappa, A. C. Cino, E. Comini, G. Leo, and C. D. Angelis, “Second harmonic emission from dielectric nanoresonators in the absorption regime,” IEEE Photonics Technol. Lett. **35**, 505–508 (2023).
17. M. Celebrano, D. Rocco, M. Gandolfi, A. Zilli, F. Rusconi, A. Tognazzi, A. Mazzanti, L. Ghirardini, E. A. Pogna, L. Carletti *et al.*, “Optical tuning of dielectric nanoantennas for thermo-optically reconfigurable nonlinear metasurfaces,” Opt. Lett. **46**, 2453–2456 (2021).
18. F. J. Löchner, A. N. Fedotova, S. Liu, G. A. Keeler, G. M. Peake, S. Saravi, M. R. Shcherbakov, S. Burger, A. A. Fedyanin, I. Brener *et al.*, “Polarization-dependent second harmonic diffraction from resonant GaAs metasurfaces,” Acs Photonics **5**, 1786–1793 (2018).
19. R. W. Waynant, I. K. Ilev, and I. Gannot, “Mid–infrared laser applications in medicine and biology,” Philos. Trans. Royal Soc. London. Ser. A: Math. Phys. Eng. Sci. **359**, 635–644 (2001).
20. S. Kuma, Y. Miyamoto, K. Tsutsumi, N. Sasao, and S. Uetake, “Difference-frequency generation using a waveguide-PPLN crystal and its application to mid-infrared lamb-dip spectroscopy,” Opt. Lett. **38**, 2825–2828 (2013).
21. D. F. Logan, M. Giguere, A. Villeneuve, and A. S. Helmy, “Widely tunable mid-infrared generation via frequency conversion in semiconductor waveguides,” Opt. Lett. **38**, 4457–4460 (2013).
22. J. Haines, M. Gandolfi, Y. Franz, C. De Angelis, and M. Guasoni, “Mid-infrared frequency generation via intermodal difference frequency generation in AlGaAs-on-insulator waveguides,” Front. Photonics **2**, 788174 (2021).
23. G. Marino, A. S. Solntsev, L. Xu, V. F. Gili, L. Carletti, A. N. Poddubny, M. Rahmani, D. A. Smirnova, H. Chen, A. Lemaître, G. Zhang, A. V. Zayats, C. D. Angelis, G. Leo, A. A. Sukhorukov, and D. N. Neshev, “Spontaneous photon-pair generation from a dielectric nanoantenna,” Optica **6**, 1416 (2019).
24. Y. Zhang, A. Manjavacas, N. J. Hogan, L. Zhou, C. Ayala-Orozco, L. Dong, J. K. Day, P. Nordlander, and N. J. Halas, “Toward surface plasmon-enhanced optical parametric amplification (SPOPA) with engineered nanoparticles: a nanoscale tunable infrared source,” Nano letters **16**, 3373–3378 (2016).
25. W. Xie, L. Chang, H. Shu, J. C. Norman, J. D. Peters, X. Wang, and J. E. Bowers, “Ultrahigh-Q AlGaAs-on-insulator microresonators for integrated nonlinear photonics,” Opt. Express **28**, 32894–32906 (2020).
26. A. Tognazzi, K. I. Okhlopkov, A. Zilli, D. Rocco, L. Fagiani, E. Mafakheri, M. Bollani, M. Finazzi, M. Celebrano, M. R. Shcherbakov *et al.*, “Third-harmonic light polarization control in magnetically resonant silicon metasurfaces,” Opt. Express **29**, 11605–11612 (2021).
27. L. Fagiani, M. Gandolfi, L. Carletti, C. de Angelis, J. Osmond, and M. Bollani, “Modelling and nanofabrication of chiral dielectric metasurfaces,” Micro Nano Eng. **19**, 100187 (2023).
28. A. Tognazzi, M. Gandolfi, B. Li, G. Ambrosio, P. Franceschini, R. Camacho-Morales, A. C. Cino, C. Baratto, D. de Ceglia, D. Neshev *et al.*, “Opto-thermal dynamics of thin-film optical limiters based on the VO_2 phase transition,” Opt. Mater. Express **13**, 41–52 (2023).
29. D. de Ceglia, M. Gandolfi, M. A. Vincenti, A. Tognazzi, P. Franceschini, A. C. Cino, G. Ambrosio, C. Baratto, B. Li, R. Camacho-Morales *et al.*, “Transient guided-mode resonance metasurfaces with phase-transition materials,” Opt. Lett. **48**, 2961–2964 (2023).
30. A. Ronchi, P. Franceschini, P. Homm, M. Gandolfi, G. Ferrini, S. Pagliara, F. Banfi, M. Menghini, C. Giannetti *et al.*, “Light-assisted resistance collapse in a V_2O_3-based mott-insulator device,” Phys. Rev. Appl. **15**, 044023 (2021).
31. M. Gandolfi, S. Peli, M. Diego, S. Danesi, C. Giannetti, I. Alessandri, V. Zannier, V. Demontis, M. Rocci, F. Beltram *et al.*, “Ultrafast photoacoustic nanometrology of InAs nanowires mechanical properties,” The J. Phys. Chem. C **126**, 6361–6372 (2022).
32. S. Adachi, “Optical dispersion relations for GaP, GaAs, GaSb, InP, InAs, InSb, Al x Ga1- x As, and In1- x Ga x As y

P1- y," J. Appl. Phys. **66**, 6030–6040 (1989).

33. G. Agrawal, *Nonlinear Fiber Optics.*, vol. 5th (Academic Press, 2013).
34. D. Rocco, V. F. Gili, L. Ghirardini, L. Carletti, I. Favero, A. Locatelli, G. Marino, D. N. Neshev, M. Celebrano, M. Finazzi *et al.*, "Tuning the second-harmonic generation in algaas nanodimers via non-radiative state optimization," Photonics research **6**, B6–B12 (2018).
35. R. Camacho-Morales, D. Rocco, L. Xu, V. F. Gili, N. Dimitrov, L. Stoyanov, Z. Ma, A. Komar, M. Lysevych, F. Karouta *et al.*, "Infrared upconversion imaging in nonlinear metasurfaces," Adv. Photonics **3**, 036002–036002 (2021).
36. L. Leandro, R. Reznik, J. Clement, J. Repän, M. Reynolds, E. Ubyivovk, I. Shtrom, G. Cirlin, and N. Akopian, "Wurtzite algaas nanowires," Sci. Reports **10**, 735 (2020).
37. G. A. Siviloglou, S. Suntsov, R. El-Ganainy, R. Iwanow, G. I. Stegeman, D. N. Christodoulides, R. Morandotti, D. Modotto, A. Locatelli, C. De Angelis *et al.*, "Enhanced third-order nonlinear effects in optical algaas nanowires," Opt. Express **14**, 9377–9384 (2006).
38. P. R. Wiecha, A. Arbouet, C. Girard, T. Baron, and V. Paillard, "Origin of second-harmonic generation from individual silicon nanowires," Phys. Rev. B **93**, 125421 (2016).
39. L. G. Helt, M. Liscidini, and J. E. Sipe, "How does it scale? comparing quantum and classical nonlinear optical processes in integrated devices," JOSA B **29**, 2199–2212 (2012).
40. G. Marino, A. S. Solntsev, L. Xu, V. F. Gili, L. Carletti, A. N. Poddubny, M. Rahmani, D. A. Smirnova, H. Chen, A. Lemaître *et al.*, "Spontaneous photon-pair generation from a dielectric nanoantenna," Optica **6**, 1416–1422 (2019).